

www.acsmaterialsletters.org

# Raman Spectroscopy and Laser-Induced Surface Modification of Nb<sub>2</sub>CT<sub>x</sub> MXene

Andrea N. Giordano,\* Jie Jiang, Abigail Advincula, Kateryna Shevchuk, Michael S. Carey, Tyson C. Back, Yury Gogotsi, Dhriti Nepal, Ruth Pachter, and Rahul Rao\*



Cite This: ACS Materials Lett. 2024, 6, 3264-3271



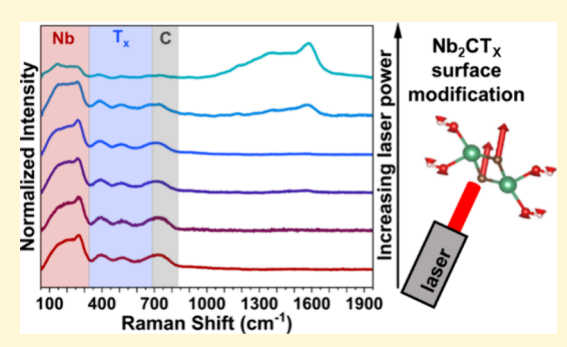
**ACCESS** I

III Metrics & More

Article Recommendations

Supporting Information

ABSTRACT: The Nb<sub>2</sub>CT<sub>x</sub> MXene has garnered interest for its potential applications in energy storage, catalysis, and sensors. Recent reports of Raman spectra of Nb<sub>2</sub>CT<sub>x</sub> reveal stark differences of the MXene incorporated into devices, which may affect the devices' performance and reproducibility. These differences illuminate a need for fundamental characterization of the Nb<sub>2</sub>CT<sub>x</sub> Raman modes to better understand the material-specific properties of the MXene integrated into devices. We conducted a comprehensive multiexcitation Raman study and observed nine Raman-active modes in Nb<sub>2</sub>CT<sub>x</sub> that are consistent with our density functional theory calculations. Additionally, we investigated laser-induced surface modification of Nb<sub>2</sub>CT<sub>x</sub> through changes in the peak intensities and frequencies, along with the generation of amorphous carbon with



increasing incident laser power. This fundamental study provides a framework to spectroscopically assess the integrity of  $Nb_2CT_x$  and a tool for creating a stable, tunable, and localized surface modification.

Xenes are a diverse class of functionalized 2D transitional metal carbides and nitrides with high electrical conductivity, large surface areas, and superb mechanical properties. They are synthesized through selective etching of the A atoms (Al, Si, Ga) from a MAX phase and follow the general formula of  $M_{n+1}X_nT_x$ , where M is an early transition metal, n = 1-4, X is carbon or nitrogen, and  $T_x$  represents surface terminal groups, such as oxygen, hydroxyl, chalcogens or halogens.<sup>1,2</sup>  $Ti_3C_2T_x$ , the flagship titanium-based MXene, has dominated the field since this material's discovery in 2011<sup>3</sup> due to its robust electrical conductivity and increasing synthetic accessibility. However, many other MXenes based on alternative transition metals have been synthesized and even more theoretically predicted. 1,4,5 Nb<sub>2</sub>CT<sub>x</sub>, a niobium-based MXene, has garnered particular interest due to its potential for applications in energy storage, biomedical devices, catalysis, and sensors due to its low ion transport barrier, favorable photocatalytic properties, hydrophilic surface, large surface area, acceptable chemical and electrochemical stabilities, and excellent mechanical flexibility.<sup>2,6-10</sup> MXenes are typically characterized using methods such as X-ray diffraction (XRD), X-ray photoelectron spectroscopy (XPS), and Raman spectroscopy, the third of which is arguably the most common technique for characterizing 2D materials. In addition to structural information, Raman spectroscopy provides insights into lattice strain and surface modification, including defects. A recent study examining the

effect of changing M or X in various MXene families (M2XTx)  $M_3X_2T_x$ , and  $M_4X_3T_x$ ) revealed several common vibrational modes, with in-plane and out-of-plane M-related phonon modes occurring at low frequencies (<300 cm<sup>-1</sup>) and broad peaks at higher-frequencies (400-700 cm<sup>-1</sup>) assigned to T<sub>r</sub> groups. 11 With regards to Raman studies specific to Nb<sub>2</sub>CT<sub>x</sub>, recent reports reveal several stark differences in the overall shape of the spectrum (i.e., number of peaks, peak positions, relative peak intensities), 11-30 which could arise from variations in composition, the quality of the starting MAX phase, the processing conditions used in etching and exfoliation, or environmental oxidation. All of these factors may impart structural differences in the resulting MXene that could affect the device performance and reproducibility; thus, there is a pressing need to resolve the vibrational modes in Nb<sub>2</sub>CT<sub>x</sub> and related materials in detail.

Herein, we performed a combined experimental and theoretical study of the phonon modes in  $Nb_2CT_x$ . We observed nine Raman-active modes, including the higher-frequency  $T_x$  phonon modes and a C-phonon mode related to

Received: April 30, 2024 Revised: May 23, 2024 Accepted: May 24, 2024 Published: June 24, 2024





vibrations in the  $\mathrm{Nb_2CT}_x$  lattice, that are consistent with our density functional theory (DFT) calculations. In examining the Raman spectra of  $\mathrm{Nb_2CT}_x$  as a function of laser power, we identified the Raman modes that are susceptible to surface modifications through changes in peak intensities and frequencies. We observed a threshold laser power above which we generated amorphous carbon. Our study provides a framework to spectroscopically assess the integrity of  $\mathrm{Nb_2CT}_x$  and a tool for creating a stable, tunable and localized surface modifications.

 $Nb_2CT_x$  Characterization.  $Nb_2CT_x$  was synthesized by etching its MAX phase, Nb2AlC, in a hydrofluoric acid solution and delamination using tetramethylammonium hydroxide (TMAOH), as described in detail in the Supporting Information (SI). The exfoliated Nb<sub>2</sub>CT<sub>x</sub> solution was dropcast on glass substrates. The as-exfoliated solution was characterized by UV-vis-NIR spectroscopy, and drop-cast films were characterized by XRD, scanning electron microscopy (SEM) with energy-dispersive X-ray spectroscopy (EDS), Raman spectroscopy, and XPS. In Figure 1a, we report the UV-vis spectrum of our Nb<sub>2</sub>CT<sub>x</sub> solution, showing a broad absorption from 700-1300 nm that is consistent with the reported literature.<sup>31</sup> The XRD pattern in Figure 1b shows a predominant (002) diffraction peak at  $2\theta = 6.7^{\circ}$  with a large dspacing of 1.3 nm caused by the elimination of Al atoms and intercalation of water and TMAOH, a key characteristic of MXenes.<sup>32</sup> Figure 1c shows an SEM image and EDS analysis with a rough quantification of the relative abundance of the atoms present from EDS analysis, including 0% Al indicating the complete removal of the MAX phase. For comparison, we have included the Raman spectrum of the Nb<sub>2</sub>AlC MAX phase in Figure S1 to accompany the XRD and EDS data demonstrating successful etching of the MAX phase.

Figure 1d shows multiexcitation Raman spectra of Nb<sub>2</sub>CT<sub>x</sub> using 514.5, 633, and 785 nm laser excitations. The overall shape of our Raman spectra are consistent with other  $M_2XT_{xy}^{11}$  but reports of Raman spectra of Nb<sub>2</sub>CT<sub>x</sub> are varied in the literature in terms of the number of peaks, peak positions, and relative peak intensties. 12-30,33 Additionally, our data does not show any laser excitation dependence of the Raman modes, unlike previous observations of resonance enhancement with the 785 nm excitation in Ti<sub>3</sub>C<sub>2</sub>T<sub>1</sub>, 34 This is in agreement with its featureless absorption spectrum in the vis-NIR range (Figure 1a). Lastly, in Figures 1e-h we report the high-resolution XPS data in the Nb 3d, O 1s, C 1s, and F 1s regions. The spectra in all four regions are consistent with the reported literature for  $Nb_2CT_x^{\phantom{1}35}$  Additionally, the relative abundance of  $T_x$  groups was determined to be 51.4% for =0, 44.4% for -OH, and 4.2% for -F terminations. The gathered characterizations give us high confidence in the etching process and quality of the Nb<sub>2</sub>CT<sub>r</sub> used for this study, precluding the possibility of artifacts arising from remaining MAX phase or other impurities.

Raman Spectrum Analysis. We calculated the Raman spectrum of an  $Nb_2CT_x$  monolayer with homogeneous terminations ( $T_x$ : =O, -OH, and -F) using DFT, including the phonon dispersions and phonon density of states (DOS). The structures (Figure S2) and computational details can be found in the SI. The calculated phonon dispersions and phonon DOS for  $Nb_2CO_2$ ,  $Nb_2C(OH)_2$ , and  $Nb_2CF_2$  are shown in Figure S3. We observe common features of the zone-center phonons for these materials. The two lowest nonzero frequency phonons (one double degenerate and one non-

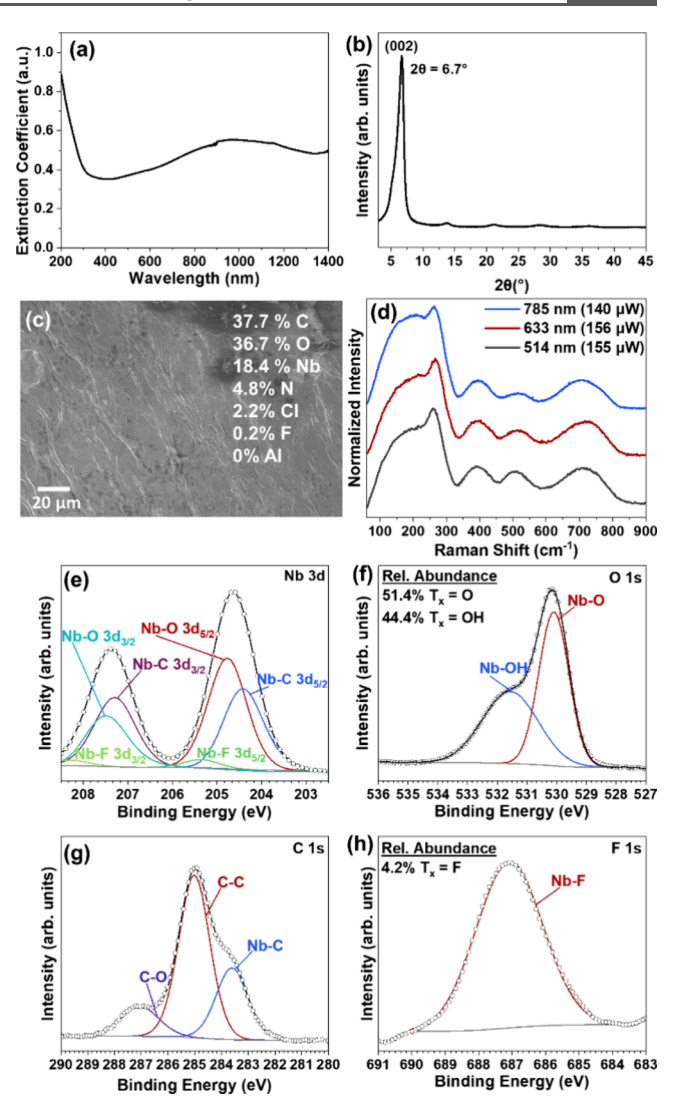


Figure 1. Characterization of  $\mathrm{Nb_2CT_{x^*}}$  (a) UV-vis-NIR spectrum of exfoliated solution, (b) XRD pattern of drop-cast film, (c) SEM image of drop-cast film with atomic composition percentages are listed in top right corner from EDS analysis (d) Raman spectra of drop-cast film at laser excitations 514.5, 633, and 785 nm. (e-h) High resolution XPS of drop-cast film for Nb 3d, O 1s, C 1s, and F 1s regions along with relative abundance of =O, -OH, and -F terminal groups.

degenerate) correspond to vibrations of the Nb atoms, while the two highest frequency phonons (one double degenerate and one nondegenerate) are attributed to C atom vibrations. The phonons at intermediate frequencies correspond to vibrations of the  $T_x$  groups.

We first discuss the four lower frequency ( $<270 \text{ cm}^{-1}$ ) Raman peaks (Figure 2a, peaks 1–4 shown in red, labeled Nb region), which we attribute to vibrational modes of the Nb atoms. The DOS calculations indicate two Raman-active vibrational modes involving Nb atoms for the =O, -OH, and -F terminated structures, respectively (Figure S3). However, since -F terminations represents only 4.2% of the  $T_x$  groups in our sample of  $Nb_2CT_x$  (Figure 1h), we consider two modes for each of the =O and -OH terminated  $Nb_2C$  structures. The peaks at 105 and 212 cm<sup>-1</sup> are attributed to phonons for  $Nb_2C(OH)_2$  (peaks 1 and 3) and peaks at 162 and 267 cm<sup>-1</sup> to phonons for  $Nb_2CO_2$  (peaks 2 and 4). The

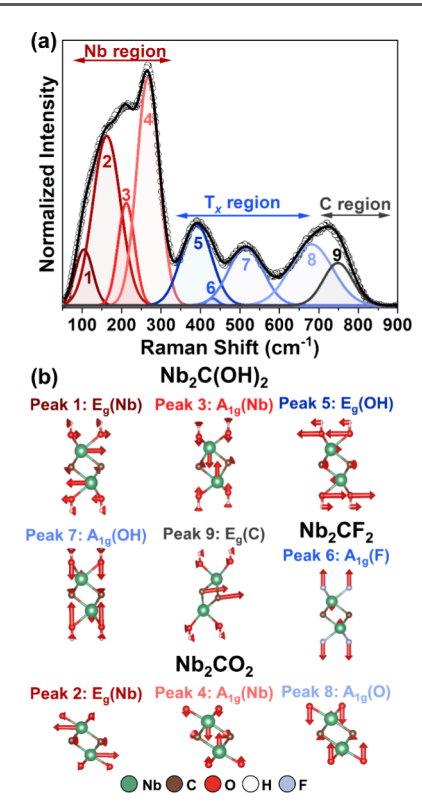


Figure 2. (a) Gaussian deconvoluted Raman spectrum of  $\mathrm{Nb_2CT_x}$ . The Nb region has four peaks shaded in red that are assigned to Nb phonon modes. The  $\mathrm{T_x}$  region has four peaks shaded in blue that are assigned to the surface terminal groups =0, -OH, and -F phonon modes. The C region has one peak shaded in gray that is assigned to the C phonon mode with -OH termination. Experimental data was collected with a 633 nm laser excitation at 217  $\mu\mathrm{W}$  power. (b) Calculated phonon modes with eigenvectors for  $\mathrm{Nb_2CT_x}$  containing =0, -OH, and -F surface terminal groups. Representative atom coloring: Nb is green, C is brown, O is red, H is white, and F is blue.

corresponding atomic displacements for these modes are shown in Figure 2b. Peaks 1 and 2 correspond to in-plane (Eg symmetry) modes and peaks 3 and 4 are out-of-plane (A $_{1g}$  symmetry) modes. The  $A_{1g}$  mode at 267 cm $^{-1}$  is the most intense peak in the Raman spectrum of Nb $_2$ CT $_x$  and occurs at similar frequencies as high-intensity modes in other  $M_2$ XT $_x$ .

Next, we turn our attention to the Raman peaks in the intermediate frequency region, i.e., peaks 5–8 in Figure 2a. By comparing the frequencies in the measured Raman spectrum to the calculated Raman-active zone-center phonons (Figure S3), we attribute the peaks at 390, 430, 515, and 681 cm $^{-1}$  to phonon modes for  $-\mathrm{OH}(E_{\mathrm{g}})$ ,  $-\mathrm{F}(A_{\mathrm{lg}})$ ,  $-\mathrm{OH}(A_{\mathrm{lg}})$ , and =  $\mathrm{O}(A_{\mathrm{lg}})$   $T_x$  groups, respectively. These assignments are illustrated in blue in Figure 2a (labeled  $T_x$  region) and their eigenvectors are depicted in Figure 2b. We note that the Raman intensity for peak 6, which is assigned to an  $A_{\mathrm{lg}}$  mode for  $-\mathrm{F}$  terminations, is significantly weaker in intensity than other  $T_x$  peaks, but is consistent with the XPS data showing only 4.2% relative abundance of the  $-\mathrm{F}$  termination (Figure 1h) and the EDS quantification showing only 0.2% F (Figure 1c).

For the highest frequency peak, we examined the calculated phonon dispersion and DOS of Nb<sub>2</sub>CO<sub>2</sub>, Nb<sub>2</sub>C(OH)<sub>2</sub>, and Nb<sub>2</sub>CF<sub>2</sub> (Figure S3). The highest frequency phonon modes originate from C vibrations, but due to symmetry, are not

Raman active for  $Nb_2CO_2$  and  $Nb_2CF_2$ . However, a phonon mode for a C vibration in  $Nb_2C(OH)_2$  is Raman active due to the lowered symmetry of the hydroxyl termination. This result indicates that by lowering the symmetry of the pristine  $Nb_2C$ , inactive modes of C vibrations can become Raman active. Therefore, the highest frequency Raman peak at 749 cm<sup>-1</sup> is attributed to the  $E_g$  phonon mode of C atoms in the  $Nb_2CT_x$  lattice (peak 9, shown in gray in Figure 2a and labeled C region). Table 1 summarizes the observed and calculated

Table 1. Experimental (633 nm Excitation and 217  $\mu$ W Laser Power) and Calculated Raman Peaks in Nb<sub>2</sub>CT<sub>x</sub>

Peak	Experimental frequency (cm <sup>-1</sup> )	Calculated frequency (cm <sup>-1</sup> )	Terminal group Nb <sub>2</sub> CX <sub>2</sub>	Phonon mode
1	105	105	ОН	Nb in-plane $(E_g)$
2	162	127	О	$\begin{array}{c} { m Nb~in} ext{-plane} \ ({ m E_g}) \end{array}$
3	212	236	ОН	Nb out-of- plane $(A_{1g})$
4	267	253	О	Nb out-of- plane $(A_{1g})$
5	390	335	ОН	OH in-plane (E <sub>g</sub> )
6	430	471	F	F out-of- plane (A <sub>1g</sub> )
7	515	512	ОН	OH out-of- plane $(A_{1g})$
8	681	546	О	O out-of- plane $(A_{1g})$
9	749	607	ОН	C in-plane $(E_g)$

Raman peaks for Nb<sub>2</sub>CT<sub>x</sub>. We note some discrepancies between experiment and theory, particularly for the higher Raman frequency peaks (Table 1), which we attribute to the material's complexity. The distribution of  $T_x$  groups on MXenes is known to be heterogeneous and has been highlighted recently by Natu et al.<sup>36</sup> Additionally, the presence of defects, possible impurities and disorder can complicate computations. We employed a rigorous theoretical approach and optimized structures that are based on careful examination of different adsorption sites, ensuring stability with no negative phonons (Table S1), and our theoretical predictions agree well with previous computations for many of the phonon modes in Nb<sub>2</sub>CT<sub>x</sub>.<sup>5</sup> However, despite the discrepancies between experiments and theory for some high frequency modes, our theoretical predictions for Nb<sub>2</sub>CT<sub>x</sub> provide important insights into the attribution of the Raman peaks to the appropriate lattice vibrations.

Laser-Induced Surface Modification. Next, we explored the effect of changing surface chemistry on the intensities and frequencies of the phonon modes in Nb<sub>2</sub>CT<sub>x</sub>. We irradiated Nb<sub>2</sub>CT<sub>x</sub> using a 633 nm laser at various incident powers from 27–5120  $\mu$ W at the sample (Table S2). We found that powers greater than 1120  $\mu$ W caused significant changes to the Nb<sub>2</sub>CT<sub>x</sub> spectra resulting in noisy and broadened peaks that could not be fit, and were therefore excluded from the analysis. It is known that MXenes oxidize under irradiation in air, producing a metal oxide and amorphous carbon. Tonsistent with the literature, we observed the formation of niobium oxide and amorphous carbon (Figure S4) at maximum incident laser power (5120  $\mu$ W). We collected and analyzed Raman spectra at 20 different incident powers ranging from

 $27-1120 \,\mu\text{W}$ . Representative spectra from this power range in the MXene region (50–900 cm<sup>-1</sup>) and the higher frequency amorphous carbon region (1200–1800 cm<sup>-1</sup>) are shown in Figures 3a and 3b, respectively. The spectra collected with

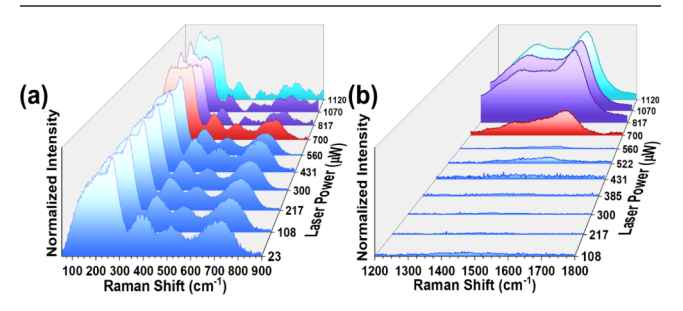


Figure 3. Raman spectra of Nb<sub>2</sub>CT<sub>x</sub> collected at 633 nm excitation with laser powers ranging from 27–1120  $\mu$ W in (a) the MXene region and (b) the amorphous carbon region. The spectra  $\leq$ 560  $\mu$ W (blue) show insignificant changes. At 700  $\mu$ W, the red spectrum shows changes in the low frequency (100–300 cm<sup>-1</sup>) and high frequency (600–800 cm<sup>-1</sup>) peaks of the MXene along with measurable D and G bands from the formation of amorphous carbon. The spectra in purple from 800–1100  $\mu$ W show significant change to all MXene peaks and an increase in the amorphous carbon formation. The spectrum in teal at 1120  $\mu$ W shows significant changes to the MXene.

incident powers  $\leq$ 560  $\mu$ W (colored blue in Figure 3) exhibit no significant changes in the MXene peaks (Figure 3a), with the most intense peak occurring at 267 cm<sup>-1</sup> (peak 4) and little to no amorphous carbon (Figure 3b). The spectrum highlighted in red at 700 µW exhibits clear changes in the low-frequency Nb peaks (peaks 1-4), where the intensity of peak 4 decreases and becomes equal to that of peak 2. Additionally, peaks 8 and 9 in the T<sub>r</sub> region start to separate and broad peaks appear between 1200-1800 cm<sup>-1</sup> signifying the formation of amorphous carbon. At higher laser powers, the spectra shown in purple (817 and 1070  $\mu$ W) reveal significant changes with peak 2 (162 cm<sup>-1</sup>) becoming the most intense peak, changes in the shape and intensity of the T<sub>x</sub> peaks, and a significant increase in the amorphous carbon peaks. At an incident laser power of 1120  $\mu$ W (teal spectrum in Figure 3), we see significant changes to the MXene peaks and the highest intensity of the amorphous carbon Raman peaks. Additionally, at laser powers >800  $\mu$ W, we observe a series of small peaks appearing in the  $T_x$  region that could be the formation of niobium oxide.3

To quantify the changes occurring in the Raman spectra of  $\mathrm{Nb_2CT_x}$  with increasing incident laser power, we deconvoluted the spectra shown in Figures 3a and 3b (Figures S5–S6 and Tables S3–S4). We analyzed the changes in peak intensity (I) and frequency  $(\omega)$  in both the MXene region and the amorphous carbon region (Figures S7–S8). In Figure 4a, we show the changes in intensities of peaks 2, 4, 5, and 9 in the MXene region and the intensities of the amorphous carbon peaks (D and G bands, corresponding to disorder-induced peak and in-plane vibrations of  $\mathrm{sp^2}$  carbon, respectively<sup>39</sup>). In general, relative intensity changes of a Raman peak correlate with population changes of that phonon mode in the material, such that a decrease in intensity would indicate a decrease in the population of that phonon mode.

Starting with the top panel of Figure 4a, the intensity ratio of peak 2 to peak 4 ( $I_2/I_4$ ) starts to increase with incident laser powers >560  $\mu$ W, which is consistent with the spectroscopic

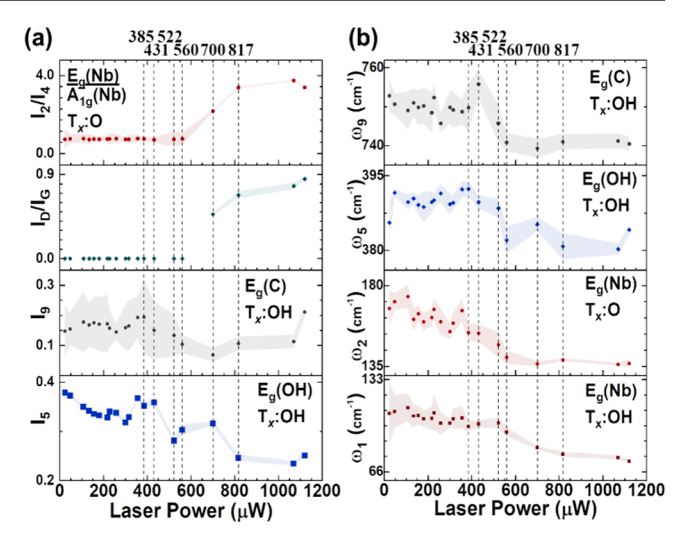


Figure 4. Analysis of Raman spectra of Nb<sub>2</sub>CT<sub>x</sub> collected at 633 nm excitation with laser powers ranging from 27–1120  $\mu$ W. (a) Analysis of normalized peak intensities of peak 5 (I<sub>5</sub>), peak 9 (I<sub>9</sub>), the intensity ratio of the D band to G band (I<sub>D</sub>/I<sub>G</sub>), and the intensity ratio of peak 2 to peak 4 (I<sub>2</sub>/I<sub>4</sub>). (b) Analysis of the peak frequencies ( $\omega$ ) of peaks 1,2,5, and 9. The shading represents the fit error on the intensity or frequency. We used dashed lines to guide the eye for incident laser powers 385–817  $\mu$ W. For reference, see Figure 2a for the Raman spectrum with peak indexing and Figure 3 for the Raman spectra of the 385–817  $\mu$ W powers.

changes in Figure 3a. The laser power dependencies of  $I_2$  and  $I_4$  are shown in Figure S7. Both  $I_2$  and  $I_4$  do not change significantly with increasing laser power up to 522  $\mu$ W, above which  $I_4$  decreases and then levels off at powers >817  $\mu$ W. The greater changes in  $I_4$  compared to  $I_2$  indicate that the  $A_{1g}$  Nb phonon mode (peak 4) is more sensitive to irradiation than the  $I_2$  Nb phonon mode (peak 2).

In the next panel in Figure 4a, we track the intensity ratio of the D and G bands  $(I_D/I_G)$  of amorphous carbon. We see a similar trend that  $I_D/I_G$  increases at incident laser powers >560  $\mu$ W, which is also consistent with the evidence of amorphous carbon formation shown in Figure 3b. The leveling off of I<sub>2</sub>/I<sub>4</sub> and I<sub>D</sub>/I<sub>G</sub> indicates that a large portion of the changes occur between  $\sim 600-800 \mu W$ . Moreover, the alignment of the trends for  $I_2/I_4$  and  $I_D/I_G$  provides evidence for the precipitation of amorphous carbon as a result of irradiation of Nb<sub>2</sub>CT<sub>x</sub>. This conclusion provides researchers a way to spectroscopically track the integrity of Nb<sub>2</sub>CT<sub>x</sub> through changes in the most intense peak and formation of amorphous carbon. In the third panel, we look at I<sub>9</sub>, the E<sub>g</sub> phonon mode associated with carbon in Nb<sub>2</sub>CT<sub>x</sub>. We observe a slight decrease in I<sub>9</sub> starting at an incident laser power of 385 µW, but the relatively large error (shaded portion) due to the broadness of the peak makes it difficult to unambiguously conclude that the amorphous carbon formation results from the carbide in the irradiated Nb<sub>2</sub>CT<sub>x</sub>.

Lastly, we examined  $I_5$  in the bottom panel of Figure 4a. We observe a net decrease in  $I_5$  over the entire incident laser power range, but with a larger decrease between 385–817  $\mu$ W, suggesting that the laser may be inducing the desorption of  $-OH\ T_x$  groups. The larger decrease in  $I_5$  between 385–817  $\mu$ W is consistent with the changes observed for  $I_2/I_4$ ,  $I_D/I_G$ , and  $I_9$ , and attributed to the onset of significant surface modification in that laser power range. As we mentioned

above, the intensity of peak 6 is small due to the lower population of -F terminal groups (4.2%) but it still decreases over the entire laser power range until it almost disappears (Figure S7). A report by Hu et al. that found only Nb<sub>2</sub>CO<sub>2</sub> was dynamically stable, while Nb<sub>2</sub>CF<sub>2</sub> and Nb<sub>2</sub>C(OH)<sub>2</sub> were dynamically unstable.<sup>5</sup> This could explain the reduction in intensity for -OH and -F terminations over the entire laser power range. In summary, the intensity changes with irradiation in the MXene and amorphous C regions provide evidence to support laser-induced surface modification of Nb<sub>2</sub>CT<sub>x</sub>, but examination of the accompanying frequency changes is warranted.

In Figure 4b, we summarize changes in the peak frequencies for peaks 1, 2, 5, 9 with incident laser power. All of the peak frequencies as a function of laser power can be found in Figure S8. In general, a shift in the frequency of a phonon mode could indicate a structural change, e.g., in bond length, bond rearrangement, or strain (tensile or compressive). Overall, we see a shift to lower frequency (red shift) for all four peaks. Starting with the top panel in Figure 4b,  $\omega_9$  is fairly consistent within error up to 385  $\mu$ W, but then a significant red shift occurs between 431–700  $\mu$ W before the frequency is consistent again. While the changes in I<sub>9</sub> were difficult to interpret owing to the large errors, but the decrease in intensity matches the power range for the red shift in frequency, suggesting that the changes in peak 9 occur from modification of the C phonon mode.

The next panel in Figure 4b shows a significant red shift for  $\omega_5$  between 385–817  $\mu$ W, which is consistent with its largest intensity decrease (bottom panel, Figure 4a) and supports the case for surface modification in this power range. In the third panel of Figure 4b,  $\omega_2$  decreases up to 700  $\mu W$  before remaining constant as it approaches the frequency for niobium oxide,<sup>38</sup> indicating the formation of the metal oxide. Lastly, in the bottom panel,  $\omega_1$  red shifts over the entire laser power range but shows the largest decrease between 522-817  $\mu$ W. The shift of these in-plane phonon modes could arise from bond lengthening, bond rearrangement, or strain induced by surface modification this material. A previous report found that tensile strain caused frequency shifts for Ti<sub>3</sub>C<sub>2</sub>T<sub>x</sub> on average of ~3.3 cm<sup>-1</sup> per% strain applied for an out-of-plane mode through mechanical testing. 40 In Figure 4b, the red shifts range from 4-39 cm<sup>-1</sup>, which is a larger shift than expected from strain resulting from surface modification.

Several factors could account for the observed frequency shifts in Figure 4b, including localized heating through the photothermal effect<sup>12</sup> and the removal of intercalated species (water and TMAOH). We performed a temperature-dependent Raman study which showed that the photothermal contribution due to varying laser power is relatively small and cannot fully account for the large red shifts observed in Figure 4b (discussion in the SI, Figure S9). To explore the contributions of the removal of intercalated species to the observed frequency shifts, we investigated the presence of water (Figure 1f) and TMAOH (Figure S10). We did not find a significant presence of water or TMAOH (discussed further in the SI), reducing the likelihood for the removal of intercalated species contributing significantly to the observed frequency shifts.

As alternative contributions to the frequency shifts did not fully explain our data, we believe the observed large red shifts result from the loss of surface functionalities and partial oxidation, leading to bond strains, defects, atomic rearrangements, and disruptions to the C network in Nb<sub>2</sub>CT<sub>x</sub>. Additionally, we observe blue shifts at higher laser power for peaks 3, 6, and 7 (Figure S8). In comparing  $\omega_3$ ,  $\omega_6$  and  $\omega_7$  to the peaks of niobium oxides (Figure S4), we believe the blue shifts are a result of the formation of niobium oxide species, providing additional evidence for the partial oxidation of Nb<sub>2</sub>CT<sub>x</sub> under irradiation. Taking a holistic look at the intensity and frequency changes presented in Figure 4, we suggest that these changes are evidence for laser-induced surface modification of the Nb<sub>2</sub>CT<sub>x</sub> through the removal of T<sub>x</sub> groups, partial oxidation of Nb, and formation of amorphous carbon.

To further understand the impacts of surface modification on the Raman spectra of Nb<sub>2</sub>CT<sub>x</sub>, we calculated vacancy formation energies for Nb, C, and O by DFT as defined in Equation S1. The calculated formation energies are listed in Table 2 for both O-terminated and bare Nb<sub>2</sub>C. The formation

Table 2. Vacancy Formation Energy  $(E_{form})$  for O-Terminated and Bare Nb<sub>2</sub>C

Atom	$E_{ m form}  ({ m eV})$
C	1.10
Nb	4.49
O	4.50
С	2.40
Nb	2.72
	C Nb O C

energies are lower for the removal of a carbon atom compared to that of a Nb atom for both bare and terminated Nb<sub>2</sub>C. A discussion of our computed results, along with a comparison to literature reports  $^{41,42}$  is provided in the SI. Our computed results agree with our Raman experiments, where the C network is disrupted and vacancies may occur in the studied incident laser power range but Nb is not removed. Thus, the rearrangement of Nb atoms must be a result of oxidation.

To elucidate the effect of surface modification on the electronic structure, we used DFT calculations to compare pristine Nb<sub>2</sub>CO<sub>2</sub> and Nb<sub>2</sub>CO<sub>2</sub> with higher (1.14  $\times$  10<sup>14</sup>/cm²) and lower (1.61  $\times$  10<sup>13</sup>/cm²) C monovacancy densities. A discussion of these calculations is provided in the SI. Our results indicate the introduction of C-vacancies changes the electronic structure of Nb<sub>2</sub>CO<sub>2</sub>, with more significant changes occurring for higher defect densities (Figures S11(a) and S11(b)). We note that the metallicity of pristine Nb<sub>2</sub>CO<sub>2</sub> does not change when introducing a C-vacancy. Examination of the optimized structures (Figure S12) demonstrates that the distortion of two NbO hexagons above and below the C-vacancy are the cause for changes in the electronic structure.

In combining the qualitative (significant spectroscopic changes), quantitative, and calculated evidence for laser-induced surface modification, we hypothesize on the evolution of the observed surface chemistry of Nb<sub>2</sub>CT<sub>x</sub>. We believe the T<sub>x</sub> groups (especially -OH and -F) are perturbed first, as we see changes in the spectra in the broadest laser power range. With the partial loss of surface functionality, the niobium atoms are vulnerable to partial oxidation, as seen with shifts of  $\omega_2$ ,  $\omega_3$ ,  $\omega_6$ ,  $\omega_7$  toward niobium oxide frequencies. The changes to the surface chemistry of Nb<sub>2</sub>CT<sub>x</sub> cause disruptions in the carbon network as seen by changes in I<sub>9</sub>,  $\omega_9$ , I<sub>2</sub>/I<sub>4</sub>, and I<sub>D</sub>/I<sub>G</sub> between laser powers 431–817  $\mu$ W. Due to the much lower vacancy formation energy of C compared to Nb, we attribute the decrease in I<sub>4</sub> to a disruption in the carbon network as

opposed to the vacancy of Nb atoms. This conclusion is also supported by the identical trends for  $\rm I_2/I_4$ , and  $\rm I_D/I_G$  (Figure 4a). In a discussion in the SI, we evaluated extrinsic carbon sources (environmental hydrocarbons, intercalated TMAOH) based on experimental evidence (Figure S10 & S14) and literature reports.  $^{37,43}$  Our experiments eliminated significant contribution from extrinsic carbon sources to the formation of amorphous carbon, therefore, the observed changes in  $\rm I_9$  and  $\omega_9$  along with a lower vacancy formation energy for C, suggest that the source of amorphous carbon is from Nb<sub>2</sub>CT<sub>x</sub>.

Lastly, we assessed the aging of surface modified  $\mathrm{Nb_2CT}_x$  by collecting Raman spectra (Figure S13) from an area initially irradiated with 700  $\mu\mathrm{W}$  and the same area 5 months later. The Raman spectra exhibit similar line shapes, indicating the stability of the surface modification. In addition, neighboring regions were investigated by Raman spectra (Figure S13) from areas 1.5–1000  $\mu\mathrm{m}$  away from the laser irradiated area 5 months prior. The Raman spectra appear identical to the pristine  $\mathrm{Nb_2CT}_x$ , indicating that the surface modification is localized to the laser spot, and exposure to air did not induce any further changes. The stability and localization of the laser-induced surface modification of  $\mathrm{Nb_2CT}_x$  thus provides researchers with a tool for creating stable, tunable and localized surface functionalization.

In conclusion, we observed nine Raman active phonon modes for Nb<sub>2</sub>CT<sub>x</sub> through the deconvolution of its Raman spectrum guided by DFT calculations. Additionally, we investigated the dependence of the Raman spectrum of Nb<sub>2</sub>CT<sub>x</sub> with incident laser power. We found that the integrity of Nb<sub>2</sub>CT<sub>x</sub> can be tracked through a significant decrease in the intensity of the most intense peak accompanied by an increase in amorphous carbon peaks. We also analyzed the peak intensities and frequencies and found a threshold power (385– 522  $\mu$ W) for surface modification of Nb<sub>2</sub>CT<sub>x</sub>. To provide additional insight into the surface modification, we calculated the vacancy formation energies in bare Nb<sub>2</sub>C and Nb<sub>2</sub>CO<sub>2</sub> and found a lower formation energy for a C-vacancy compared to Nb. The effect of a C monovacancy on the calculated band structure of Nb<sub>2</sub>CO<sub>2</sub> showed changes to the electronic structure, while preserving its metallicity. Using the qualitative, quantitative, and computed evidence for the laser-induced surface modification of Nb<sub>2</sub>CT<sub>x</sub>, we hypothesize that the T<sub>x</sub> groups are disrupted first, followed by partial oxidation of vulnerable Nb atoms causing a disruption to the carbon network and the formation of amorphous carbon. This study provides a fundamental framework to characterize Nb<sub>2</sub>CT<sub>x</sub> using Raman spectroscopy, serves as a guide to the spectroscopical assessment of the structural integrity, and provides a tool for creating a stable, tunable, and localized surface modification.

# ASSOCIATED CONTENT

# **5** Supporting Information

The Supporting Information is available free of charge at https://pubs.acs.org/doi/10.1021/acsmaterialslett.4c00922.

Methods section, Raman spectrum of Nb<sub>2</sub>AlC MAX phase, Nb<sub>2</sub>CT<sub>x</sub> monolayer structures, phonon dispersion, DOS, calculated incident laser power densities, Raman spectrum of Nb<sub>2</sub>CT<sub>x</sub> at maximum laser power, Nb<sub>2</sub>CT<sub>x</sub> peak fits, Nb<sub>2</sub>CT<sub>x</sub> peak fitting parameters; analysis of intensity and frequency changes, temperature-dependent Raman spectra, Raman spectra TMAOH,

band structures for pristine and single C vacancy  $8 \times 8 \times 81$  and  $3 \times 3 \times 1$  supercells, optimized  $8 \times 8 \times 1$  and  $3 \times 3 \times 1$  supercells, Raman spectra after 5 months of aging, and Raman spectra under vacuum (PDF)

## AUTHOR INFORMATION

## **Corresponding Authors**

Andrea N. Giordano — Materials and Manufacturing Directorate, Air Force Research Laboratory, Wright-Patterson Air Force Base, Ohio 45433, United States; National Research Council, Washington, D.C. 20001, United States; orcid.org/0000-0001-6668-7747;

Email: andrea.giordano.2.ctr@us.af.mil

Rahul Rao — Materials and Manufacturing Directorate, Air Force Research Laboratory, Wright-Patterson Air Force Base, Ohio 45433, United States; orcid.org/0000-0002-6415-0185; Email: rahul.rao.2@us.af.mil

#### **Authors**

Jie Jiang – Materials and Manufacturing Directorate, Air Force Research Laboratory, Wright-Patterson Air Force Base, Ohio 45433, United States

Abigail Advincula — Materials and Manufacturing Directorate, Air Force Research Laboratory, Wright-Patterson Air Force Base, Ohio 45433, United States; ARCTOS, Beavercreek, Ohio 45432, United States; UES, Inc., Dayton, Ohio 45432, United States

Kateryna Shevchuk — A. J. Drexel Nanomaterials Institute and Department of Materials Science and Engineering, Drexel University, Philadelphia, Pennsylvania 19104, United States; orcid.org/0000-0001-7411-3110

Michael S. Carey – Materials and Manufacturing Directorate, Air Force Research Laboratory, Wright-Patterson Air Force Base, Ohio 45433, United States; Riverside Research Institute, Dayton, Ohio 45431, United States

Tyson C. Back – Materials and Manufacturing Directorate, Air Force Research Laboratory, Wright-Patterson Air Force Base, Ohio 45433, United States

Yury Gogotsi — A. J. Drexel Nanomaterials Institute and Department of Materials Science and Engineering, Drexel University, Philadelphia, Pennsylvania 19104, United States; orcid.org/0000-0001-9423-4032

Dhriti Nepal — Materials and Manufacturing Directorate, Air Force Research Laboratory, Wright-Patterson Air Force Base, Ohio 45433, United States; Orcid.org/0000-0002-0972-9960

Ruth Pachter — Materials and Manufacturing Directorate, Air Force Research Laboratory, Wright-Patterson Air Force Base, Ohio 45433, United States; orcid.org/0000-0003-3790-4153

Complete contact information is available at: https://pubs.acs.org/10.1021/acsmaterialslett.4c00922

# **Author Contributions**

The manuscript was written through the contributions of all authors. All authors have approved the final version of the manuscript. CRediT: **Andrea N. Giordano** conceptualization, data curation, formal analysis, visualization, writing-original draft, writing-review & editing; **Jie Jiang** data curation, formal analysis, writing-original draft, writing-review & editing; **Abigail Advincula** data curation, methodology, writing-original draft, writing-review & editing; **Kateryna Shevchuk** data

curation, writing-review & editing; Michael S. Carey data curation, writing-original draft, writing-review & editing; Tyson C. Back data curation, writing-review & editing; Yury Gogotsi resources, supervision, writing-review & editing; Dhriti Nepal conceptualization, supervision, writing-review & editing; Ruth Pachter conceptualization, methodology, supervision, writing-review & editing; Rahul Rao conceptualization, formal analysis, supervision, visualization, writing-review & editing.

## **Funding**

A.N.G acknowledges support in part by the appointment to the NRC Research Associateship Program at the Air Force Research Laboratory, administered by the Fellowships Office of the National Academies of Sciences, Engineering, and Medicine. Y.G acknowledges support from the US National Science Foundation (grant DMR-2041050) for collaboration with AFRL. D. N. acknowledges support from Air Force Office of Scientific Research (22RXCOR014).

## **Notes**

The authors declare no competing financial interest.

## ACKNOWLEDGMENTS

The authors would like to thank Ryan Selhorst for help with microscopy, Josh Yoho for assistance with neutral density filters for varying laser power, Dylan Slizewski for feedback on figure design, and Kyle Matthews for help with MXene synthesis.

## ABBREVIATIONS

XRD, X-ray diffraction; SEM, scanning electron microscopy; EDS, energy dispersive X-ray spectroscopy; XPS, X-ray photoelectron spectroscopy; DFT, density functional theory; DOS, density of states; TMAOH, tetramethylammonium hydroxide

# REFERENCES

- (1) VahidMohammadi, A.; Rosen, J.; Gogotsi, Y. The World of Two-Dimensional Carbides and Nitrides (MXenes). *Science* **2021**, *372*, eabf1581.
- (2) Anasori, B.; Lukatskaya, M. R.; Gogotsi, Y. 2D Metal Carbides and Nitrides (MXenes) for Energy Storage. *Nat. Rev. Mater.* **2017**, *2*, 16098.
- (3) Naguib, M.; Kurtoglu, M.; Presser, V.; Lu, J.; Niu, J.; Heon, M.; Hultman, L.; Gogotsi, Y.; Barsoum, M. W. Two-Dimensional Nanocrystals Produced by Exfoliation of Ti<sub>3</sub>AlC<sub>2</sub>. *Adv. Mater.* **2011**, 23, 4248–4253.
- (4) Yorulmaz, U.; Özden, A.; Perkgöz, N. K.; Ay, F.; Sevik, C. Vibrational and Mechanical Properties of Single Layer MXene Structures: A First-Principles Investigation. *Nanotechnology* **2016**, 27, 335702.
- (5) Hu, T.; Hu, M.; Gao, B.; Li, W.; Wang, X. Screening Surface Structure of MXenes by High-Throughput Computation and Vibrational Spectroscopic Confirmation. *J. Phys. Chem. C* **2018**, 122, 18501–18509.
- (6) Ramachandran, T.; Mourad, A.-H. I.; ElSayed, M. S. A. Nb<sub>2</sub>CT<sub>x</sub>-Based MXenes Most Recent Developments: From Principles to New Applications. *Energies* **2023**, *16*, 3520.
- (7) Rasheed, P. A.; Pandey, R. P.; Banat, F.; Hasan, S. W. Recent Advances in Niobium MXenes: Synthesis, Properties, and Emerging Applications. *Matter* **2022**, *5*, 546–572.
- (8) Naguib, M.; Halim, J.; Lu, J.; Cook, K. M.; Hultman, L.; Gogotsi, Y.; Barsoum, M. W. New Two-Dimensional Niobium and Vanadium Carbides as Promising Materials for Li-Ion Batteries. *J. Am. Chem. Soc.* **2013**, *135*, 15966–15969.

- (9) Xu, X.; Zhang, C.; Yin, J.; Smajic, J.; Bahabri, M.; Lei, Y.; Hedhili, M. N.; Hota, M. K.; Shi, L.; Guo, T.; Zheng, D.; El-Demellawi, J. K.; Lanza, M.; Costa, P. M. F. J.; Bakr, O. M.; Mohammed, O. F.; Zhang, X.; Alshareef, H. N. Anisotropic nisotropic Superconducting Nb<sub>2</sub>CT<sub>x</sub> MXene Processed by Atomic Exchange at the Wafer Scale. *Adv. Mater.* **2024**, *36*, 2305326.
- (10) Thomas, S. A.; Cherusseri, J. A Review of  $\mathrm{Nb_2CT_x}$  MXene as an Emerging 2D Material: Synthesis, Applications in Rechargeable Batteries and Supercapacitors, Progress, and Outlook. *Energy Fuels* **2023**, *37*, 7555–7576.
- (11) Shevchuk, K.; Sarycheva, A.; Shuck, C. E.; Gogotsi, Y. Raman Spectroscopy Characterization of 2D Carbide and Carbonitride MXenes. *Chem. Mater.* **2023**, *35*, 8239–8247.
- (12) Lin, H.; Gao, S.; Dai, C.; Chen, Y.; Shi, J. A Two-Dimensional Biodegradable Niobium Carbide (MXene) for Photothermal Tumor Eradication in NIR-I and NIR-II Biowindows. *J. Am. Chem. Soc.* **2017**, 139, 16235–16247.
- (13) Yuan, Z.; Wang, L.; Li, D.; Cao, J.; Han, W. Carbon-Reinforced Nb<sub>2</sub>CT<sub>x</sub> MXene/MoS<sub>2</sub> Nanosheets as a Superior Rate and High-Capacity Anode for Sodium-Ion Batteries. *ACS Nano* **2021**, *15*, 7439–7450.
- (14) Xiao, J.; Yu, P.; Gao, H.; Yao, J. Endogenous  $Nb_2CT_x/Nb_2O_5$  Schottky Heterostructures for Superior Lithium-Ion Storage. *J. Colloid Interface Sci.* **2023**, 652, 113–121.
- (15) Su, T.; Peng, R.; Hood, Z. D.; Naguib, M.; Ivanov, I. N.; Keum, J. K.; Qin, Z.; Guo, Z.; et al. One Step Synthesis of Nb<sub>2</sub>O<sub>5</sub>/C/Nb<sub>2</sub>C (MXene) Composites and Their Use as Photocatalysts for Hydrogen Evolution. *ChemSusChem* **2018**, *11*, 688–699.
- (16) Makola, L. C.; Moeno, S.; Ouma, C. N. M.; Sharma, A.; Vo, D.-V. N.; Dlamini, L. N. Facile Fabrication of a Metal-Free <sup>2</sup>D-<sup>2</sup>D Nb<sub>2</sub>CT<sub>x</sub>@g-C<sub>3</sub>N<sub>4</sub> MXene-Based Schottky-Heterojunction with the Potential Application in Photocatalytic Processes. *J. Alloys Compd.* **2022**, *916*, 165459.
- (17) Du, L.; Duan, H.; Xia, Q.; Jiang, C.; Yan, Y.; Wu, S. Hybrid Charge Storage Route to Nb<sub>2</sub>CT<sub>x</sub> MXene as Anode for Sodium Ion Batteries. *ChemistrySelect* **2020**, *5*, 1186–1192.
- (18) Huang, J.; Tao, J.; Liu, G.; Lu, L.; Tang, H.; Qiao, G. In Situ Construction of 1D CdS/2D Nb<sub>2</sub>CT<sub>x</sub> MXene Schottky Heterojunction for Enhanced Photocatalytic Hydrogen Production Activity. *Appl. Surf. Sci.* **2022**, *573*, 151491.
- (19) Rajavel, K.; Yu, X.; Zhu, P.; Hu, Y.; Sun, R.; Wong, C. Investigation on the Structural Quality Dependent Electromagnetic Interference Shielding Performance of Few-Layer and Lamellar Nb<sub>2</sub>CT<sub>x</sub> MXene Nanostructures. *J. Alloys Compd.* **2021**, 877, 160235.
- (20) Shabana, N.; Arjun, A. M.; Ankitha, M.; Rasheed, P. A. Nb<sub>2</sub>CT<sub>x</sub>@MoS<sub>2</sub> Composite as a Highly Efficient Catalyst for the Degradation of Organic Dyes. *Catal. Commun.* **2023**, *173*, 106566.
- (21) Song, S.; Liu, J.; Zhou, C.; Jia, Q.; Luo, H.; Deng, L.; Wang, X. Nb<sub>2</sub>O<sub>5</sub>/Nb<sub>2</sub>CT<sub>x</sub>Composites with Different Morphologies through Oxidation of Nb<sub>2</sub>CT<sub>x</sub> MXene for High-Performance Microwave Absorption. *J. Alloys Compd.* **2020**, *843*, 155713.
- (22) Zhang, M.; Yin, H.; Jin, F.; Liu, J.; Ji, X.; Du, A.; Yang, W.; Liu, Z. Vacancy Engineering of Oxidized Nb<sub>2</sub>CT<sub>x</sub> MXenes for a Biased Nitrogen Fixation. *Green Energy Environ.* **2023**, *8*, 1185–1194.
- (23) Zhao, Y.; Hao, H.; Zhong, J.; Jiang, S.; Zhang, G.; Bi, J.; Yan, S.; Hou, H. Photothermocatalytic Sterilization Performance and Mechanism of Pure Nb<sub>2</sub>CT<sub>x</sub> MXenes Nanosheets under Infrared Light Irradiation. *Appl. Surf. Sci.* **2023**, *613*, 155990.
- (24) Arjun, A. M.; Shabana, N.; Ankitha, M.; Rasheed, P. A. Electrochemical Deposition of Prussian Blue on Nb<sub>2</sub>CT<sub>x</sub> Mxene Modified Carbon Cloth For the Non-Enzymatic Electrochemical Detection of Hydrogen Peroxide. *Microchem. J.* **2022**, *185*, 108301.
- (25) Li, X.; Li, N.; Huang, Z.; Chen, Z.; Liang, G.; Yang, Q.; Li, M.; Zhao, Y.; Ma, L.; Dong, B.; Huang, Q.; Fan, J.; Zhi, C. Enhanced Redox Kinetics and Duration of Aqueous  $I_2/I^-$  Conversion Chemistry by MXene Confinement. *Adv. Mater.* **2021**, 33, 2006897.
- (26) Huang, S.; Mochalin, V. N. Understanding Chemistry of Two-Dimensional Transition Metal Carbides and Carbonitrides (MXenes) with Gas Analysis. *ACS Nano* **2020**, *14*, 10251–10257.

- (27) Bi, M.; Miao, Y.; Li, W.; Yao, J. Niobium Carbide MXene-Optics Fiber-Sensor for High Sensitivity Humidity Detection. *Appl. Phys. Lett.* **2022**, *120*, 021103.
- (28) Li, W.; Miao, Y.; Zheng, Y.; Zhang, K.; Yao, J. Nb<sub>2</sub>CT<sub>x</sub> MXene Integrated Tapered Microfiber Based on Light-Controlled Light for Ultra-Sensitive and Wide-Range Hemoglobin Detection. *IEEE Sens. J.* **2022**, 22, 11456–11462.
- (29) Din Babar, Z. U.; Fatheema, J.; Arif, N.; Anwar, M. S.; Gul, S.; Iqbal, M.; Rizwan, S. Magnetic Phase Transition from Paramagnetic in Nb<sub>2</sub>AlC-MAX to Superconductivity-like Diamagnetic in Nb<sub>2</sub>C-MXene: An Experimental and Computational Analysis. *RSC Adv.* **2020**, *10*, 25669–25678.
- (30) Song, M.; Pang, S.-Y.; Guo, F.; Wong, M.-C.; Hao, J. Fluoride-Free 2D Niobium Carbide MXenes as Stable and Biocompatible Nanoplatforms for Electrochemical Biosensors with Ultrahigh Sensitivity. *Adv. Sci.* **2020**, *7*, 2001546.
- (31) Maleski, K.; Shuck, C. E.; Fafarman, A. T.; Gogotsi, Y. The Broad Chromatic Range of Two-Dimensional Transition Metal Carbides. *Adv. Opt. Mater.* **2021**, *9*, 2001563.
- (32) Han, M.; Shuck, C. E.; Rakhmanov, R.; Parchment, D.; Anasori, B.; Koo, C. M.; Friedman, G.; Gogotsi, Y. Beyond  $\mathrm{Ti}_3\mathrm{C}_2\mathrm{T}_x$ : MXenes for Electromagnetic Interference Shielding. *ACS Nano* **2020**, *14*, 5008–5016.
- (33) Gao, L.; Ma, C.; Wei, S.; Kuklin, A. V.; Zhang, H.; Ågren, H. Applications of Few-Layer Nb<sub>2</sub>C MXene: Narrow-Band Photodetectors and Femtosecond Mode-Locked Fiber Lasers. *ACS Nano* **2021**, *15*, 954–965.
- (34) Lioi, D. B.; Neher, G.; Heckler, J. E.; Back, T.; Mehmood, F.; Nepal, D.; Pachter, R.; Vaia, R.; Kennedy, W. J. Electron-Withdrawing Effect of Native Terminal Groups on the Lattice Structure of  ${\rm Ti}_3{\rm C}_2{\rm T}_x$  MXenes Studied by Resonance Raman Scattering: Implications for Embedding MXenes in Electronic Composites. *ACS Appl. Nano Mater.* **2019**, *2*, 6087–6091.
- (35) Halim, J.; Cook, K. M.; Naguib, M.; Eklund, P.; Gogotsi, Y.; Rosen, J.; Barsoum, M. W. X-Ray Photoelectron Spectroscopy of Select Multi-Layered Transition Metal Carbides (MXenes). *Appl. Surf. Sci.* **2016**, 362, 406–417.
- (36) Natu, V.; Barsoum, M. W. MXene Surface Terminations: A Perspective. J. Phys. Chem. C 2023, 127, 20197–20206.
- (37) Sarycheva, A.; Gogotsi, Y. Raman Spectroscopy Analysis of the Structure and Surface Chemistry of  $Ti_3C_2T_x$  MXene. *Chem. Mater.* **2020**, 32, 3480–3488.
- (38) Hossain, N.; Günes, O.; Zhang, C.; Koughia, C.; Li, Y.; Wen, S.-J.; Wong, R.; Kasap, S.; Yang, Q. Structural and Physical Properties of NbO<sub>2</sub> and Nb<sub>2</sub>O<sub>5</sub> Thin Films Prepared by Magnetron Sputtering. *J. Mater. Sci. Mater. Electron.* **2019**, *30*, 9822–9835.
- (39) Ferrari, A. C.; Robertson, J. Interpretation of Raman Spectra of Disordered and Amorphous Carbon. *Phys. Rev. B* **2000**, *61*, 14095–14107.
- (40) Liu, M.; Zhuo, Y.; Sarycheva, A.; Gogotsi, Y.; Bissett, M. A.; Young, R. J.; Kinloch, I. A. Deformation of and Interfacial Stress Transfer in Ti<sub>3</sub>C<sub>2</sub> MXene-Polymer Composites. *ACS Appl. Mater. Interfaces* **2022**, *14*, 10681–10690.
- (41) Gouveia, J. D.; Gomes, J. R. B. Structural and Energetic Properties of Vacancy Defects in MXene Surfaces. *Phys. Rev. Mater.* **2022**, *6*, 024004.
- (42) Ibragimova, R.; Rinke, P.; Komsa, H.-P. Native Vacancy Defects in MXenes at Etching Conditions. *Chem. Mater.* **2022**, 34, 2896–2906.
- (43) Tang, J.; Mathis, T. S.; Kurra, N.; Sarycheva, A.; Xiao, X.; Hedhili, M. N.; Jiang, Q.; Alshareef, H. N.; Xu, B.; Pan, F.; Gogotsi, Y. Tuning the Electrochemical Performance of Titanium Carbide MXene by Controllable In Situ Anodic Oxidation. *Angew. Chem., Int. Ed.* 2019, 58, 17849–17855.